

## Comparative Study of Electrostatic Models for the Amide-I and -II Modes: Linear and Two-Dimensional Infrared Spectra

Hiroaki Maekawa and Nien-Hui Ge\*

Department of Chemistry, University of California at Irvine, Irvine, California 92697-2025

Received: September 8, 2009; Revised Manuscript Received: November 19, 2009

We have carried out a comparative study of five ab initio electrostatic frequency maps and a semiempirical model for the amide-I and -II modes. Unrestrained molecular dynamics simulation of a  $3_{10}$ -helical peptide, Z-Aib-L-Leu-(Aib)<sub>2</sub>-Gly-OtBu, in CDCl<sub>3</sub> is performed using the AMBER ff99SB force field, and the linear and two-dimensional infrared (2D IR) spectra are simulated on the basis of a vibrational exciton Hamiltonian model. A new electrostatic potential-based amide-I and -II frequency map for *N*-methylacetamide is developed in this study. This map and other maps developed by different research groups are applied to calculate the local mode frequencies of the amide linkages in the hexapeptide. The simulated amide-I line shape from all models agrees well with the previous experimental results on the same system, except for an overall frequency shift. In contrast, the simulated amide-II bands are more sensitive to the frequency maps. Essential features obtained in the electrostatic models are captured by the semiempirical model that takes into account only the intramolecular hydrogen bonding effects and solvent shifts. Detailed comparisons between the models are also drawn through analysis of the local mode frequency shifts. Among all of the maps tested in this study, the new four-site potential map performs quite well in simulating the amide-II bands. It properly predicts the effects of hydrogen bonding on the amide-I and -II frequencies and reasonably simulates the isotope-dependent amide-I/II cross peaks upon <sup>13</sup>C= <sup>18</sup>O/<sup>15</sup>N substitutions.

### I. Introduction

Vibrational modes characteristic to a peptide linkage are referred to as the amide modes, and there are seven amide modes whose atomic motions are well-characterized in normal-mode analysis of *N*-methylacetamide (NMA), the simplest model compound of peptide linkages.<sup>1</sup> The amide-I mode mostly consists of the highly localized C=O stretching motion and is known to be sensitive to peptide and protein conformation. Spectral analysis of the amide-I band in linear infrared (IR) and vibrational circular dichroism (VCD) measurements has often been utilized to characterize the basic secondary structures and their content in proteins.<sup>1–3</sup> Recent intensive application of two-dimensional (2D) IR spectroscopy<sup>4–6</sup> also focuses on the amide-I modes in different secondary structures, such as  $\alpha$ -helix,<sup>7,8</sup>  $3_{10}$ -helix,<sup>9–13</sup> antiparallel  $\beta$ -sheet,<sup>14,15</sup> and  $\beta$ -hairpin,<sup>16–18</sup> as well as some proteins in aqueous solutions<sup>19</sup> and membranes,<sup>20</sup> and aggregated amyloid peptides.<sup>21,22</sup> It has also been recognized that 2D IR spectroscopy is a promising tool for monitoring dynamical structure change in time scales from picosecond to millisecond.<sup>19,23</sup> Isotope substitution of the amide-I modes with <sup>13</sup>C= <sup>16</sup>O and <sup>13</sup>C= <sup>18</sup>O enables the linear and nonlinear spectroscopic methods to selectively probe structure and dynamics at a specific local position.<sup>8,12,16–18,20,21,24,25</sup>

Other amide modes have also attracted attention in spectroscopic studies. For example, the amide-A mode, ascribed to the N–H stretching mode, can be used to investigate intra- and intermolecular hydrogen bonding because hydrogen bonding produces drastic changes in the resonant frequency and absorption cross section of the mode.<sup>1</sup> Mirkin and Krimm found from their DFT calculation of alanine dipeptide (*N*-acetyl-L-alanine-*N*'-methylamide) and tripeptide that the amide-III mode was

sensitive to dihedral angles  $\phi$  and  $\psi$ .<sup>26</sup> The amide-II mode, mainly composed of the C–N stretching mode and the out-of-phase, in-plane N–H bending mode, has also been used to study molecular conformation by linear IR and VCD.<sup>1–3,27</sup> Especially, the significant frequency shift ( $\sim$ 100 cm<sup>−1</sup>) upon deuteration makes the amide-II mode a useful reporter of the H/D exchange process, from which detailed information on kinetics and structure stability of biological macromolecules has been extracted.<sup>28</sup> Recently, 2D IR spectroscopy has also been applied to the amide-II mode. The amide-I/II and -II/II vibrational couplings (or -I'/II' and -II'/II' when the peptide units are nitrogen-deuterated) of NMA,<sup>29–31</sup> peptides,<sup>12,32–34</sup> and proteins<sup>35,36</sup> have been investigated. Of particular interest are two recent studies<sup>12,34</sup> that demonstrated that the cross-peaks between the amide-I and -II modes connected through an intramolecular C=O $\cdots$ H–N hydrogen bond are discernible with the aid of <sup>13</sup>C and <sup>18</sup>O labeling on the amide-I mode and <sup>15</sup>N labeling on the amide-II mode.<sup>12,34</sup> The demonstrated strategy is a promising method toward detecting the formation of a single helical turn from an extended polypeptide chain. These new studies demonstrated further the potential of 2D IR spectroscopy and demanded a theoretical advancement to properly simulate spectral patterns of the amide-I and -II modes.

Compared with many theoretical studies on the local mode frequency<sup>37–47</sup> and nearest-neighbor coupling<sup>33,48–51</sup> of the amide-I modes, the amide-II mode has not been extensively studied yet. Only a few groups have expanded the calculation protocol to create local mode frequency maps<sup>31,33,52</sup> and coupling maps<sup>33,34,53</sup> for the amide-II modes. These vibrational properties were calculated for peptide linkages in small model peptide compounds, such as NMA and Ac-Gly-NHMe. Therefore, it is necessary to check whether they are applicable to peptides and proteins to properly reproduce the linear and nonlinear responses

\* To whom correspondence should be addressed. Phone: 949-824-1263. Fax: 949-824-8571. E-mail: nhge@uci.edu.

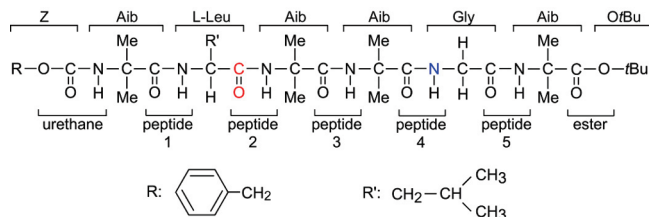


**Figure 1.** Structural formula of Z-Aib-L-Leu-(Aib)<sub>2</sub>-Gly-Aib-OrBu (**1**). The carbonyl carbon and oxygen atoms shown in red in the second peptide unit are labeled with <sup>13</sup>C= <sup>18</sup>O in the monolabeled peptide (**1\***). The nitrogen atom shown in blue in the fourth peptide unit is labeled with <sup>15</sup>N in the bis-labeled peptide (**1\*\***), in addition to the <sup>13</sup>C= <sup>18</sup>O label in the second unit.

using, for example, a vibrational exciton model. Several critical tests have been carried out for the amide-I modes based on the 2D IR spectra simulated with the molecular dynamics (MD) simulation in explicit solvent molecules.<sup>13,47,54</sup> In these comparative studies, different electrostatic and empirical models for the local site energies were compared by simulating 2D IR spectra of some proteins<sup>54</sup> and membrane peptide bundles<sup>47</sup> in aqueous solutions, and a L-( $\alpha$ Me)Val  $3_{10}$ -helical octapeptide in deuterated chloroform.<sup>13</sup>

To test the transferability of the different electrostatic frequency maps created for the amide-II mode of NMA, we conduct a comparative study on their performance in simulating the amide-I/II 2D IR spectra of a  $3_{10}$ -helical hexapeptide, Z-Aib-L-Leu-(Aib)<sub>2</sub>-Gly-OrBu (**1**, Z, benzyloxycarbonyl; Aib, C<sup>α,ω</sup>-dimethylglycine; OrBu, *tert*-butoxy, Figure 1) in CDCl<sub>3</sub>. Previous 2D IR measurements revealed that the peptide forms the  $3_{10}$ -helix structure,<sup>12,34</sup> as expected for Aib-rich oligopeptides in a relatively weak polar solvent such as chloroform.<sup>55,56</sup> Due to methylation of the  $\alpha$ -carbon, the energetically favorable conformations around the Aib residue are highly restrained to the helical region of the Ramachandran plot ( $\phi \sim \pm 60 \pm 20^\circ$ ,  $\psi \sim \pm 30 \pm 20^\circ$ ).<sup>57</sup> This propensity leads to a relatively stable  $3_{10}$ - or  $\alpha$ -helix structure for an Aib-rich peptide in the crystal state and solution phases.<sup>55,56</sup> If MD simulation is able to predict this structural homogeneity, a short peptide with a robust conformation is a desirable model in the comparative study of 2D IR spectra because we can rule out the possibility that disagreement between the measured and simulated spectra originates from poor performance of the MD force field. In our previous study on (Z)-[L-( $\alpha$ Me)Val]<sub>8</sub>-OrBu in CDCl<sub>3</sub>, the adapted CHARMM22 force field generated a trajectory with a relatively high population of  $\alpha$ -helical and nonhelical conformations in an unrestrained NVE MD simulation,<sup>13</sup> contrary to several experimental results that indicate that the peptide most likely forms a  $3_{10}$ -helix.<sup>9,10,58,59</sup> The simulated 2D IR spectral patterns based on the unrestrained trajectory disagreed with those observed in measurements, and a restrained trajectory referenced to the  $3_{10}$ -helix crystal structure was required to achieve much better agreement.<sup>13</sup> In this study, we employ the AMBER force field (ff99SB)<sup>60–62</sup> to get a trajectory of the Aib-rich peptide. Several different force fields, such as CHARMM,<sup>63</sup> GROMOS,<sup>64,65</sup> and Cedar,<sup>66</sup> have been applied to Aib-rich peptides to study the relative stability of  $\alpha$ -,  $3_{10}$ -, and  $\pi$ -helical conformations in gas and solution phases. The most stable helical conformations obtained from these simulations are quite dependent on the force fields used. It is intriguing to see whether the structure sampled by the AMBER force field can simulate the measured 2D IR spectra, which is very sensitive to peptide helicity.<sup>13</sup>

To model both the amide-I and -II modes, we newly create a four-site electrostatic potential map in this study to compare

with the four existing electrostatic maps: three of the six-site electrostatic potential maps by Bouč et al.<sup>52</sup> and the four-site electrostatic field/gradient map by Bloem et al.<sup>31</sup> The comparison provides insights into how the performance depends on the basis set, density functional, the number of parametrized sites, and electrostatic model.

Although the previous study<sup>34</sup> reasonably well reproduced the experimental 2D IR spectra of **1** and its <sup>13</sup>C= <sup>18</sup>O-Leu monolabeled (**1\***) and <sup>13</sup>C= <sup>18</sup>O-Leu/<sup>15</sup>N-Gly bis-labeled (**1\*\***) isotopomers using a model calculation based on the ideal  $3_{10}$ -helix conformation and a semiempirical model for the amide-I and -II local site energies, some subtle features observed for the amide-II band were still missing. In addition, the <sup>15</sup>N isotope effects on the amide-II spectral features were less quantitatively reproduced. Thus, another objective in this study is to check whether the combined computation protocol of MD simulation and more sophisticated electrostatic models is able to better reproduce the measured amide-I and -II 2D IR spectra than the semiempirical model.

This paper is organized as follows: Details on the MD simulation, spectral simulation, and features of the different electrostatic models are given in the next section. Our semiempirical model and the newly created DFT frequency maps for the amide-I and -II modes are also included. Section III presents the results of MD trajectory analysis and local mode frequency calculation, and the simulated linear IR and 2D IR rephasing (R) and nonrephasing (NR) spectra of the unlabeled hexapeptide **1**. The spectra of the <sup>13</sup>C= <sup>18</sup>O- and <sup>15</sup>N-labeled peptides (**1\*** and **1\*\***) are simulated using the frequency maps that best reproduced the amide-I and -II bands of **1**. We discuss the performance of the electrostatic models on the basis of their ability to reasonably predict the frequency shifts and reproduce the linear and 2D IR spectra, especially of the amide-II mode. Concluding remarks are given in the Section IV.

## II. Methods

**A. MD Simulation.** A nanosecond MD trajectory of **1** in CDCl<sub>3</sub> was obtained with the NAMD simulation program package<sup>67</sup> and the modified AMBER force field (ff99SB), which has been shown to achieve a better balance of secondary structure elements than other force fields.<sup>60–62</sup> Partial charges of the unnatural amino acid residue, Aib, as well as the capping groups (Z and OrBu) were determined by the restrained electrostatic potential (RESP) method following the same method as in the original determination.<sup>60,68</sup> These values are presented in Figure 2. During the fitting process for the Aib residue, the partial charges of the C, O, N, and H atoms that will participate in the peptide linkages with other residues were fixed to 0.5973e, -0.5679e, -0.4157e and 0.2719e (e is the elementary charge), the same values as the other natural amino acid residues in the AMBER force field.<sup>60</sup> The charges of Aib determined in this study are slightly different from those determined by Ramos and co-workers,<sup>69</sup> perhaps because no charge restraints were applied in their study.

A rectangular box (60 Å × 49 Å × 46 Å) containing one peptide and 845 CDCl<sub>3</sub> molecules was equilibrated for ~3.5 ns before a 1.5-ns production run under three-dimensional periodic boundary conditions. Constant temperature and pressure (293 K and 1 atm) of the system were regulated by the Langevin dynamics method with a damping coefficient of 5 ps<sup>-1</sup><sup>70</sup> and Langevin piston Nosé-Hoover barostat,<sup>70,71</sup> respectively. Because there are no structure data available for this peptide, we set its initial conformation to the ideal right-handed  $3_{10}$ -helix with ( $\phi, \psi$ ) = (-57°, -30°), and the positions of the backbone C<sup>α</sup>

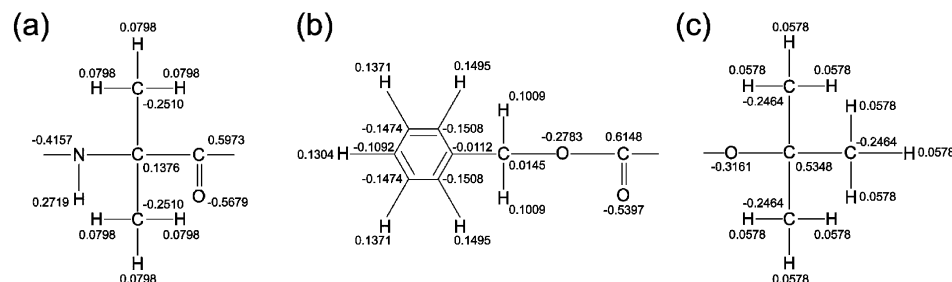


**Figure 2.** Partial charges of the unnatural amino acid residue (a) Aib ( $\text{C}^{\alpha,\alpha}\text{-dimethylglycine}$ ) and protecting groups (b) Z (benzyloxycarbonyl) and (c)  $\text{OtBu}$  (*tert*-butoxy) determined by the RESP method. Bond lengths in these schematic pictures are not to scale.

atoms were harmonically restrained during only the equilibration process. Electrostatic interaction was calculated using the particle-mesh Ewald sum method.<sup>72</sup> All bond lengths involving hydrogen atoms were constrained using the SHAKE algorithm.<sup>73</sup> The trajectory was calculated with a 2-fs time step, and 15 000 snapshots were sampled at every 0.1 ps along the 1.5-ns trajectory for the analysis of molecular conformations, hydrogen bonding patterns, and the site energies of the amide-I/II modes to compute their linear and 2D IR spectra.

**B. Electrostatic and Semiempirical Models.** Five different electrostatic models and one semiempirical model are compared below.

Bouř et al. reported an electrostatic potential model with six parametrization sites on C, O, N, H, C(-C), and C(-N) for the amide-I, -II, -III and -A modes.<sup>52</sup> Their three different sets of parameters were based on DFT calculations of NMA-3H<sub>2</sub>O clusters at the three different levels of BPW91/6-31G\*\*, BPW91/6-311++G\*\*, and B3LYP/6-311++G\*\* and correlating the vibrational frequencies with the electrostatic potential created by the water molecules. Ten cluster configurations were generated from MD simulation with the AMBER force field, and the potential was modeled by atomic partial charges of water (0.42e for hydrogen and -0.84e for oxygen). We applied these maps to the local mode frequency calculation and denote them as models B1 (BPW91/6-31G\*\*), B2 (BPW91/6-311++G\*\*), and B3 (B3LYP/6-311++G\*\*). It should be noted that our MD simulation was performed using the AMBER force field, and hence, the calculated local amide mode frequencies are expected to have fewer systematic errors that may come from different charges used in the MD simulation and the creation of DFT maps.

The amide-I' and -II' frequencies of NMA-*d* were correlated with electric fields and their gradients at the amide C, O, N, and D atoms by Knoester and co-workers<sup>31</sup> on the basis of DFT calculation with the ADF TZ2P basis and the RPBE exchange correlation functional. The map coefficients were fitted to 16 components of electric fields and gradients created in 75 different point charge configurations. The frequencies estimated from their electrostatic map had a correlation factor of 0.97 for the amide-I' mode and 0.90 for the amide-II' mode. It is noted that the map was scaled to give the correct gas phase frequencies; namely, 1717 cm<sup>-1</sup> for the amide-I' and 1440 cm<sup>-1</sup> for the amide-II' mode. Although the latter is lower by ~60 cm<sup>-1</sup> from that of NMA due to the exchanged deuterium, we used their map without additional rescaling and denote it as the model K.

In the previous study,<sup>13</sup> the four-site potential model parameterized at the amide C, O, N, and H atoms of NMA by Cho and co-workers<sup>41</sup> reasonably reproduced the observed amide-I, R and NR spectral patterns of the  $\text{Z-}[\text{L-(}\alpha\text{Me)Val}]_8\text{-OrBu}$  in  $\text{CDCl}_3$ . This frequency map was constructed for only the amide-I mode on the basis of ab initio

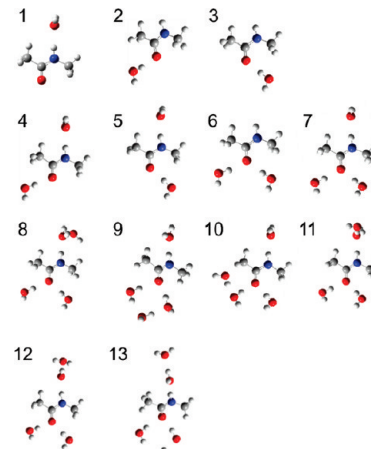


**Figure 3.** Optimized structures of *N*-methylacetamide/*n*-D<sub>2</sub>O complexes (*n* = 1–5) obtained from DFT calculations at the B3LYP/6-31+G\* level.

calculation of 96 NMA-*n*D<sub>2</sub>O (*n* = 1–5) complexes at the RHF/6-311++G\*\* level.<sup>41</sup> However, parameters for the amide-II mode were not reported. The need to model the amide-II mode stimulated us to create a four-site potential map on our own to see whether the spectral features of the amide-II mode can be predicted as well as those of the amide-I mode.

Our potential map was created in a similar way to Cho's except that the electrostatic potential was correlated with the frequencies obtained by DFT calculations at the B3LYP/6-31+G\* level, and 13 NMA/D<sub>2</sub>O complexes with different intermolecular configurations were considered. DFT calculations were carried out using the Gaussian03 package.<sup>74</sup> The optimized structures of NMA-nD<sub>2</sub>O ( $n = 1-5$ ) are presented in Figure 3. First, we performed normal mode analysis of an isolated NMA in vacuum and obtained a scaling factor by fitting the calculated amide-I and -II mode frequencies to the experimental gas phase values ( $\omega_0^{I(II)}$ ) of 1723 and 1499 cm<sup>-1</sup>,<sup>38</sup> respectively. This factor was used to scale the amide-I and -II frequencies of the NMA/D<sub>2</sub>O complexes, and the shift ( $\delta\omega^{I(II)}$ ) of the scaled frequency ( $\omega^{I(II)}$ ) from  $\omega_0^{I(II)}$  was correlated with electrostatic potentials from the surrounding water molecules:

$$\delta\omega^{\text{I(II)}} = \omega^{\text{I(II)}} - \omega_0^{\text{I(II)}} = 116140.8 \sum_i \sum_k l_i^{\text{I(II)}} \frac{q_k}{|r_i - r_k|} \quad (1)$$

where  $i$  represents the four parametrized sites of NMA (that is, the amide C, O, N, and H atoms) and  $k$  represents the atoms of water molecules. The partial charges  $q_D = 0.412e$  and  $q_O = -0.824e$  were used to calculate electrostatic potentials created by the atoms at a distance of  $|r_i - r_k|$  (in Å) away from the

**TABLE 1: Correlation Parameters  $\bar{l}_i^{(II)}$  (as a fraction of  $e$ ) between the Electrostatic Potential at the Four Amide Atom Sites (C, O, N, and H) and the Amide-I and Amide-II Frequency Shifts, as Determined in the Model G**

parametrized site	amide-I	amide-II
C	0.011 79	0.012 70
O	-0.007 56	-0.002 46
N	-0.005 49	-0.008 76
H	0.001 26	-0.001 48

parametrized site. The correlation coefficients  $\bar{l}_i^{(II)}$  are listed in Table 1, and the sum of  $\bar{l}_i^{(II)}$  is zero. As shown in Figure 4, the DFT frequency of the amide-I and -II mode is reproduced to within  $\pm 5 \text{ cm}^{-1}$ . It is well known that hydrogen bonding at the oxygen and hydrogen atom decreases (increases) the amide-I (II) mode frequency.<sup>37–40</sup> In addition, the hydrogen-bond-induced amide-I frequency shift is larger at the carbonyl site than at the N–H site. This trend is the opposite in the case of the amide-II mode: A larger shift is caused by hydrogen-bonding at the N–H group than at the carbonyl group. These characteristics are clearly seen in the one-to-one complexes (Figure 3, 1–3). We denote our four-site potential maps as the model G to compare with the other models.

It is worthwhile to apply the semiempirical model (Em) that was devised in the previous study of the hexapeptides,<sup>34</sup> where the major experimental features were reproduced by simply assuming that all residues have the same average dihedral angles ( $\phi, \Psi$ ) = ( $-57^\circ, -30^\circ$ ) with Gaussian standard deviations of  $\sim 9.5^\circ$ . In Em, the intramolecular C=O $\cdots$ H–N hydrogen bonding is considered as the only source from the peptide that induces frequency shifts of the amide-I and -II modes. Hydrogen bond electrostatic energies are calculated at the amide C=O and N–H sites separately, and they are converted to the frequency shifts by the factors of  $\kappa_{\text{CO}}^{\text{I}} = 0.42 \text{ cm}^{-1} \text{ mol kJ}^{-1}$ ,  $\kappa_{\text{NH}}^{\text{I}} = 0.96 \text{ cm}^{-1} \text{ mol kJ}^{-1}$ ,  $\kappa_{\text{CO}}^{\text{II}} = -0.70 \text{ cm}^{-1} \text{ mol kJ}^{-1}$ , and  $\kappa_{\text{NH}}^{\text{II}} = -2.9 \text{ cm}^{-1} \text{ mol kJ}^{-1}$ , where  $\kappa_{\text{CO}}^{\text{I/II}}$  and  $\kappa_{\text{NH}}^{\text{I/II}}$  are conversion factors for the amide-I (II) mode when hydrogen bonding occurs at the C=O and N–H sites, respectively. Solvent contributions are also empirically included by considering the two amide C=O groups that are exposed to CDCl<sub>3</sub> at the C-terminus. The amide-I (II) frequency of the last two linkages was shifted by  $-10$  (+5)

cm<sup>-1</sup> with a standard deviation of  $7.5$  (5) cm<sup>-1</sup>. Because CDCl<sub>3</sub> molecules do not form hydrogen bonds with N–H groups, it is reasonable to ignore the effects on the first N–H group at the N-terminus.

All of the electrostatic models described above were built on the basis of NMA or NMA-d. The frequency shifts were correlated with electrostatic potentials from the surrounding water molecules or electrostatic field/gradient from external charges, and the two methyl groups of NMA do not contribute to the calculation of electrostatic properties. When these maps are used to calculate the local mode frequencies of a peptide unit in polypeptides, it is necessary to define a “chromophore”; that is, a group of atoms whose potential, field, and gradient are excluded from the calculation of the local mode frequency shift.

Following the same definition used in the previous simulation studies for the amide-I mode,<sup>13,54,75</sup> we defined the chromophore as the minimum group of atoms that contains the parametrized atoms and maintains charge neutrality within the group. Table 2 depicts the chromophore and parametrized atoms in each model. In the AMBER force field, the partial charges of amino acid residues have been determined so that their total sum gives a net charge of zero.<sup>60</sup> Thus, the chromophore as defined in the six-site models (B1, B2, and B3) requires excluding two complete residues in the frequency shift calculation. For the four-site models, it is possible to define the chromophore in three different ways. The chromophore of models K and G contains two complete residues. In addition to the parametrized atoms, the model KN chromophore includes the C<sup>a</sup> atom and the side chain groups on the N-terminal side, whereas the model KC chromophore includes those on the C-terminal side.

**D. Computation of Linear and 2D IR Spectra.** We calculated the linear and 2D IR spectra by a combination of the vibrational exciton model and a sum-over-states approach. Vibrational exciton Hamiltonian for the amide-I and -II modes was built for each snapshot of the MD trajectory with the local mode frequencies as the diagonal elements and the intermode couplings as the off-diagonal elements. The nearest-neighbor couplings between the amide-I/I, -I/II, -II/I, and -II/II modes have been mapped out as a function of  $\phi$  and  $\psi$  in the DFT calculation for Ac-Gly-NHMe,<sup>34</sup> and the corresponding values were read out for the nearest-neighbored local modes in the peptide. The coupling between the amide-I/II modes in the same peptide linkage was set to  $-33 \text{ cm}^{-1}$ ,<sup>34</sup> close in magnitude to the experimentally determined values for NMA ( $27 \text{ cm}^{-1}$  in DMSO<sup>29</sup> and  $29 \text{ cm}^{-1}$  in D<sub>2</sub>O<sup>30</sup>) and a proline dipeptide ( $29.6$ – $32 \text{ cm}^{-1}$ ).<sup>76</sup> All of the other couplings were approximated by the transition charge coupling.<sup>34</sup> The two-exciton Hamiltonian was built from the one-exciton Hamiltonian under the harmonic approximation. The diagonal anharmonicities of the amide-I and -II modes were set to  $16$  and  $11 \text{ cm}^{-1}$ , respectively.<sup>30,77</sup> The urethane and ester C=O stretching modes and the urethane vibration similar to the amide-II mode were also included in the simulation, as described previously.<sup>34</sup> The amide-I and -II frequencies of the second peptide unit in **1\*** and **1\*\*** were decreased by  $69$  and  $8 \text{ cm}^{-1}$ , respectively, to account for the isotope effect of <sup>13</sup>C=<sup>18</sup>O labeling. The amide-II frequency of the forth peptide unit in **1\*\*** was red-shifted by  $16 \text{ cm}^{-1}$  to account for the <sup>15</sup>N isotope shift based on the experimentally observed shift for iPrCO-Gly-OtBu.<sup>34</sup> The transition dipoles of the amide-I and -II local modes and capping groups have been defined in our previous study.<sup>34</sup> Because not all existing models provide correlation maps that can be used to predict vibrational anharmonicity and dipole strength from electrostatic properties,

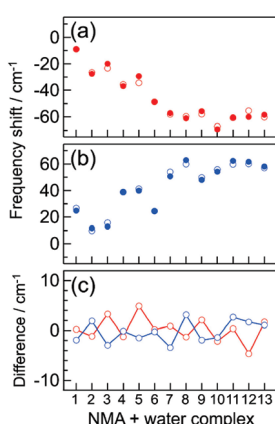


**Figure 4.** The amide-I (a) and amide-II (b) mode frequency shift of N-methylacetamide solvated with 1–5 D<sub>2</sub>O molecules: (filled circles) DFT calculation results at the B3LYP/6-31+G(d) level; (open circles) frequency shifts calculated based on eq 1 of the four-site electrostatic potential model G. The differences between the DFT and the four-site potential model calculation of the amide-I (red) and amide-II (blue) mode are presented in (c). The numbering of the NMA/D<sub>2</sub>O complexes corresponds to the optimized configurations shown in Figure 3.

**TABLE 2: Description of the Models; Definition of Chromophore and Parameterized Atoms; and Solvent, Peptide, and Total Frequency Shift of the Amide-I and -II Local Modes**

model	chromophore and parameterized atoms <sup>a</sup>	ref	linkage	amide-I frequency shift <sup>b</sup>					amide-II frequency shift <sup>b</sup>				
				1	2	3	4	5	1	2	3	4	5
B1 <sup>c</sup> potential 6-site		52	solvent	-9.9 (6.4)	-13.5 (7.1)	-14.4 (7.1)	-18.9 (7.9)	-16.3 (9.0)	-0.4 (4.6)	-4.0 (5.6)	-0.2 (5.6)	-0.1 (6.6)	3.1 (7.2)
			peptide	9.4 (6.3)	9.4 (6.8)	3.5 (7.5)	14.4 (7.8)	17.4 (5.8)	30.7 (5.6)	47.2 (6.2)	37.9 (6.6)	38.6 (5.7)	37.1 (6.2)
			total	-0.5 (8.6)	-4.0 (9.6)	-10.9 (10.0)	-4.5 (10.6)	1.1 (10.0)	30.3 (6.8)	43.2 (7.5)	37.7 (8.1)	38.5 (8.3)	40.2 (9.0)
			solvent	-7.3 (4.2)	-8.9 (4.6)	-9.8 (4.7)	-13.2 (5.6)	-10.1 (6.2)	-8.6 (10.8)	-19.2 (13.0)	-21.2 (12.3)	-27.1 (13.5)	-29.1 (15.1)
			peptide	-0.2 (4.1)	-10.6 (7.4)	-5.6 (8.2)	0.7 (9.0)	-15.3 (6.2)	35.3 (12.3)	76.6 (12.9)	71.6 (13.5)	88.5 (13.7)	99.4 (12.8)
			total	-7.6 (5.6)	-16.3 (6.5)	-19.5 (6.6)	-15.4 (7.3)	-12.5 (7.7)	26.7 (15.9)	57.4 (17.2)	50.4 (17.7)	61.5 (18.1)	70.2 (18.0)
			solvent	-6.1 (3.7)	-7.0 (4.2)	-8.3 (4.3)	-11.9 (5.5)	-9.4 (6.0)	-6.2 (9.0)	-11.2 (10.5)	-6.6 (10.8)	-5.9 (12.0)	-2.9 (13.8)
			peptide	-9.0 (4.1)	-19.3 (4.9)	-18.5 (5.0)	-11.0 (4.3)	-11.7 (4.2)	58.1 (11.3)	87.8 (11.8)	65.1 (12.6)	66.7 (12.5)	67.7 (11.6)
			total	-15.1 (5.2)	-26.3 (6.4)	-26.8 (6.4)	-22.8 (6.9)	-21.0 (7.8)	51.9 (14.0)	76.5 (15.1)	58.6 (16.1)	60.8 (16.5)	64.9 (16.4)
K <sup>f</sup> field/ gradient 4-site		31	solvent	-4.9 (4.2)	-6.0 (4.9)	-7.5 (5.3)	-11.1 (6.6)	-9.8 (6.6)	1.0 (2.8)	0.6 (3.3)	1.6 (3.1)	2.9 (3.8)	3.8 (3.8)
			peptide	-17.2 (5.3)	-22.2 (7.1)	-19.3 (7.3)	-4.9 (7.8)	-8.4 (6.4)	13.8 (3.1)	16.7 (4.1)	14.1 (4.4)	9.1 (4.3)	11.2 (3.7)
			total	-22.1 (6.4)	-28.3 (8.3)	-26.8 (8.6)	-16.1 (10.0)	-18.2 (9.2)	14.7 (4.0)	17.4 (5.0)	15.7 (5.2)	12.1 (5.5)	15.0 (5.1)
			solvent	-4.9 (4.2)	-6.0 (4.9)	-7.5 (5.3)	-11.1 (6.6)	-9.8 (6.6)	1.0 (2.8)	0.6 (3.3)	1.6 (3.1)	2.9 (3.8)	3.8 (3.8)
			peptide	-24.6 (8.1)	33.9 (8.7)	36.3 (9.1)	28.5 (8.9)	44.4 (7.2)	-7.1 (5.6)	-21.9 (6.0)	-24.4 (5.8)	-13.7 (4.5)	-29.4 (5.9)
			total	-29.5 (8.9)	27.9 (9.6)	28.8 (10.0)	17.4 (10.8)	34.7 (9.1)	-6.1 (6.2)	-21.2 (6.5)	-22.8 (6.5)	-10.7 (5.8)	-25.6 (6.9)
			solvent	-4.9 (4.2)	-6.0 (4.9)	-7.5 (5.3)	-11.1 (6.6)	-9.8 (6.6)	1.0 (2.8)	0.6 (3.3)	1.6 (3.1)	2.9 (3.8)	3.8 (3.8)
			peptide	15.5 (7.9)	-28.4 (9.6)	11.5 (9.2)	29.2 (10.4)	-12.2 (7.0)	-4.1 (5.3)	-9.4 (5.4)	-1.3 (4.6)	-5.6 (5.3)	-17.5 (3.7)
			total	10.6 (8.7)	-34.4 (10.5)	4.0 (10.2)	18.1 (12.0)	-21.9 (8.9)	-3.1 (6.0)	-8.8 (6.2)	0.3 (5.6)	-2.7 (6.4)	-13.7 (5.2)
G <sup>g</sup> potential 4-site		this study	solvent	-5.5 (3.9)	-8.2 (4.2)	-7.9 (4.6)	-12.9 (6.1)	-8.7 (6.5)	2.5 (4.3)	-1.0 (4.9)	2.5 (5.0)	1.2 (5.3)	3.7 (6.1)
			peptide	-8.2 (4.8)	-11.5 (5.6)	-10.3 (4.9)	1.0 (3.6)	-3.3 (3.2)	11.5 (5.5)	34.8 (7.2)	33.1 (7.8)	37.5 (7.5)	30.0 (6.1)
			total	-13.6 (5.8)	-19.7 (6.9)	-18.2 (6.4)	-11.9 (7.1)	-12.0 (7.5)	14.0 (6.7)	33.8 (8.4)	35.5 (8.9)	38.7 (8.9)	33.6 (8.5)
			solvent	0.0 (0.0)	0.0 (0.0)	0.0 (0.0)	-10.0 (7.5)	-10.0 (7.5)	0.0 (0.0)	0.0 (0.0)	0.0 (0.0)	5.0 (3.0)	5.0 (3.0)
			peptide	-19.8 (4.9)	-30.8 (5.6)	-25.8 (6.0)	-9.6 (2.2)	-7.6 (2.4)	6.2 (1.5)	31.6 (6.2)	29.8 (6.3)	27.1 (6.3)	21.3 (6.8)
			total	-19.8 (4.9)	-30.8 (5.6)	-25.8 (6.0)	-24.6 (5.5)	-22.6 (5.5)	6.2 (1.5)	31.6 (6.2)	29.8 (6.3)	32.1 (7.0)	26.3 (7.4)
			solvent	0.0 (0.0)	0.0 (0.0)	0.0 (0.0)	-10.0 (7.5)	-10.0 (7.5)	0.0 (0.0)	0.0 (0.0)	0.0 (0.0)	5.0 (3.0)	5.0 (3.0)
			peptide	-19.8 (4.9)	-30.8 (5.6)	-25.8 (6.0)	-9.6 (2.2)	-7.6 (2.4)	6.2 (1.5)	31.6 (6.2)	29.8 (6.3)	27.1 (6.3)	21.3 (6.8)
			total	-19.8 (4.9)	-30.8 (5.6)	-25.8 (6.0)	-24.6 (5.5)	-22.6 (5.5)	6.2 (1.5)	31.6 (6.2)	29.8 (6.3)	32.1 (7.0)	26.3 (7.4)

<sup>a</sup> The parameterized atoms are in shown red. <sup>b</sup> The frequency shift (in  $\text{cm}^{-1}$ ) is averaged over 15 000 snapshots along the 1.5-ns MD trajectory. The numbers in parentheses represent the standard deviations of the frequency shifts. <sup>c</sup> DFT calculation at the level of BPW91/6-31G\*\*. <sup>d</sup> DFT calculation at the level of BPW91/6-311++G\*\*. <sup>e</sup> DFT calculation at the level of B3LYP/6-311++G\*\*. <sup>f</sup> DFT calculation with TZ2P basis and the RPBE exchange correlation function. <sup>g</sup> DFT calculation at the level of B3LYP/6-31+G\*.

we employed only the correlation maps for the local mode frequency in this comparative study.

Diagonalization of the one- and two-exciton Hamiltonian gives the transition frequencies and dipole moments between the exciton states. These properties, together with the line width and orientational factors, are fundamental to determine the spectral pattern of linear and 2D IR spectra. In addition, the structural inhomogeneity as sampled by MD snapshots causes additional line broadening due to inhomogeneity of the local mode frequencies and vibrational couplings. It was concluded in the previous simulation study that the former was especially dominant for the amide-I spectra.<sup>13,54</sup> In the simulation below, the fast and slow line-broadening effects were assumed to be

separable for both of the amide-I and -II modes. We used a Lorentzian function with a half width at half-maximum of 6  $\text{cm}^{-1}$  to model the homogeneous line shape and sampled 15 000 snapshots from the NPT MD trajectory to take into account the inhomogeneous contributions. The formulas to calculate the linear and 2D IR spectra<sup>10,11</sup> and the orientational factors for the perpendicular polarization<sup>15</sup> have already been reported.

The calculation protocol described above involves static averages over MD snapshots without extracting dynamics directly from the MD simulations. This approach has been applied by a number of groups to simulate amide-I 2D IR spectra.<sup>6,13,18,54,78</sup> It is adequate for simulating 2D spectra at a very short waiting time,  $T$ , when the effects of dynamical

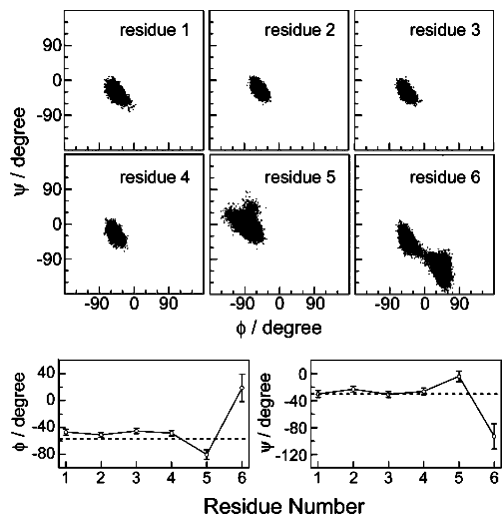


**Figure 5.** Dihedral angles ( $\phi$ ,  $\psi$ ) of **1** in  $\text{CDCl}_3$  extracted from the 1.5-ns MD trajectory. The bottom panels show the average and standard deviation of  $\phi$  (left) and  $\psi$  (right) at each residue. The angles of the ideal  $3_{10}$ -helix structure,  $\phi = -57^\circ$  and  $\psi = -30^\circ$ , are indicated by the dashed lines.

**TABLE 3: Average ( $\phi_{\text{ave}}$ ,  $\psi_{\text{ave}}$ ) and Standard Deviation ( $\sigma_\phi$ ,  $\sigma_\psi$ ) of Dihedral Angles Obtained from the 1.5-ns MD Trajectory Analysis of **1** in  $\text{CDCl}_3$  (in degrees)**

residue	$\phi_{\text{ave}}$	$\sigma_\phi$	$\psi_{\text{ave}}$	$\sigma_\psi$
1	-46.9	8.7	-30.1	10.3
2	-50.9	7.3	-23.2	8.9
3	-45.1	7.7	-30.9	9.2
4	-48.6	7.7	-26.4	10.3
5	-80.2	14.8	-4.1	15.8
6	-43.6	10.5	-39.9	15.2
	43.6	10.8	-114.4	17.0

processes, such as spectral diffusion, vibrational energy transfer, and chemical exchange, are not prominent. Recently, several methods in the time domain have been developed to take into account these dynamics and are more suitable for simulating waiting time dependence of 2D IR spectra.<sup>79–81</sup>

### III. Results and Discussion

**A. Analysis of MD Trajectory.** Molecular conformation of the 1.5-ns MD trajectory was analyzed in terms of dihedral angles and the pattern of  $\text{C}=\text{O}\cdots\text{H}-\text{N}$  intramolecular hydrogen bonding. Figure 5 plots the dihedral angle distribution for each pair of  $\phi$  and  $\psi$ . The statistical averages and standard deviations are shown in the bottom panels and also tabulated in Table 3. The average angles around the first four residues at the N-terminus are very close to those of the ideal  $3_{10}$ -helix ( $\phi = -57^\circ$ ,  $\psi = -30^\circ$ ), and their standard deviations ( $\sigma_\phi = 7.3\text{--}8.7^\circ$  and  $\sigma_\psi = 8.9\text{--}10.2^\circ$ ) are very close to the value ( $9.5^\circ$ ) we used in the previous model calculation.<sup>34</sup> In contrast, the last two residues, Gly and Aib, highly fluctuate around the mean structure and deviate from the ideal  $3_{10}$ -helix. In particular, the last residue clearly has some population with  $(\phi, \psi) = (45^\circ, -120^\circ)$ . In the overall 1.5-ns simulation started with the ideal right-handed  $3_{10}$ -helix as the initial structure, we did not detect any occurrence of the left-handed conformation in any of the residues.

Figure 6 shows the time-dependent, intramolecular hydrogen bonding pattern of the  $\text{C}=\text{O}$  groups in the urethane and the first three peptide linkages at the N-terminus. We used the Kabsch–Sander electrostatic energy criterion of  $-0.5 \text{ kcal/mol}$  to define the existence of a hydrogen bond between the  $\text{C}=\text{O}$

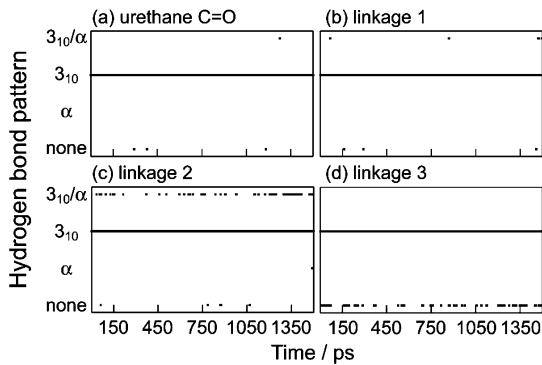


**Figure 6.** Analysis of the intramolecular  $\text{C}=\text{O}\cdots\text{H}-\text{N}$  hydrogen bonding pattern along the 1.5-ns MD trajectory of **1** in  $\text{CDCl}_3$ : (a) the urethane  $\text{C}=\text{O}$ ; the  $\text{C}=\text{O}$  in (b) the first peptide linkage, (c) the second linkage, and (d) the third linkage. The hydrogen bonding pattern is classified into  $3_{10}$  ( $i$  and  $i + 3$  residues),  $\alpha$  ( $i$  and  $i + 4$  residues)  $3_{10}/\alpha$  (bifurcated), and no bonding based on the Kabsch–Sander hydrogen bond energy criterion of  $-0.5 \text{ kcal/mol}$ .<sup>82</sup>

and  $\text{N}-\text{H}$  groups.<sup>82</sup> In agreement with the results of dihedral angle analysis above, the four  $\text{C}=\text{O}$  groups form mainly  $3_{10}$ -helical intramolecular hydrogen bonds between  $i$  and  $(i + 2)$  linkages with a tiny fraction of  $3_{10}/\alpha$  bifurcated pattern. The  $\text{C}=\text{O}$  group in the second linkage, which is labeled with  $^{13}\text{C}=^{18}\text{O}$  in **1\*** and **1\*\***, is hydrogen-bonded with the  $\text{N}-\text{H}$  group in the fourth linkage, which is labeled with  $^{15}\text{N}$  in **1\*\*** most of the time (>98%). The floppier residues at the C-terminus are probably the main reason that the  $\text{C}=\text{O}$  group in the third linkage has a slightly higher percentage of being free from hydrogen bonding. Note that there is no  $\alpha$ -helical hydrogen-bond donor to this  $\text{C}=\text{O}$  group, and hence, the  $\alpha$ -helical or  $3_{10}/\alpha$  bifurcated hydrogen bonding patterns are zero at all times.

The results shown in Figures 5 and 6 indicate that the almost ideal  $3_{10}$ -helix is the dominant conformation that the Aib-rich hexapeptide takes in  $\text{CDCl}_3$ . This conclusion drawn from the MD simulation study corroborates our structural determination that the peptide **1** forms a  $3_{10}$ -helix in  $\text{CDCl}_3$ , as concluded from the characteristic  $3_{10}$ -helix doublet cross-peak pattern in the amide-I frequency region.<sup>12</sup> We should emphasize that the simulation was implemented without any restraints imposed on the backbone conformation or side chain groups. In the previous comparative study for Z-[( $\alpha$ Me)Val]<sub>8</sub>-OtBu in  $\text{CDCl}_3$ , the unrestrained MD simulation using the CHARMM force field predicted a heterogeneous helical structure ensemble that was too broad to reproduce the experimental 2D IR spectral patterns.<sup>13</sup> Another example was shown by Kuczera and co-workers that the  $3_{10}$ -helix of the  $(\text{Aib})_{10}$  peptide was significantly less stable than the  $\alpha$ - or  $\pi$ -helix in solutions when the CHARMM22 force field was applied.<sup>63</sup> However, protected  $(\text{Aib})_{10}$  peptides form a regular  $3_{10}$ -helical conformation in the crystal state and in weakly polar solvents such as  $\text{CDCl}_3$  and DMSO.<sup>11,83,84</sup> Our result suggests that the AMBER ff99SB force field as adapted here is capable of simulating the helical conformations of Aib peptides better than the CHARMM22 force field with the previous adaptation.<sup>13,63</sup>

**B. Comparisons of Local Mode Frequencies from Different Electrostatic Models.** Before drawing detailed comparisons of linear and 2D IR spectra simulated with the different models, it is insightful to check whether there are notable differences in the calculated amide-I and -II local mode frequencies. Figure 7 shows the amide-I and -II local mode frequency shifts obtained from the eight models (B1, B2, B3, K, KN, KC, G, and Em). They are plotted in different scales to clearly reveal the variations in each model. The total frequency

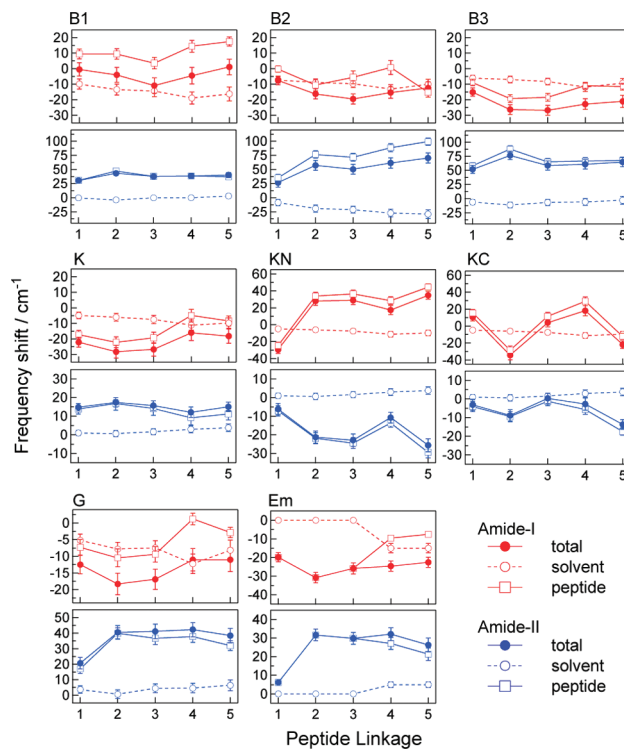


**Figure 7.** The average amide-I (red) and amide-II (blue) local mode frequency shifts calculated with the different models for the 1.5-ns MD trajectory of **1** in  $\text{CDCl}_3$ : frequency shift contribution from  $\text{CDCl}_3$  molecules (open circles); frequency shift contribution from the peptide backbone and side chain atoms outside the chromophore (squares); and the total frequency shifts (filled circles). The standard deviations of each component are indicated by the vertical bars. See Table 2 and text for the details of each model.

shift is separated into the contributions from the solvent and from the peptide atoms outside the chromophore. The mean values and standard deviations are also summarized in Table 2. The calculated frequencies exhibit a significant dependence on models; namely, the electrostatic properties (potential or field/gradient), the number of parametrization atom, procedure, basis set and functional used in the DFT calculation, and the definition of chromophore.

First, comparisons among the models B1, B2, and B3 are made. For the amide-I mode, the three models show that the solvent shift (open circles) is  $-6$  to  $-19 \text{ cm}^{-1}$  and varies little over the residues. Interestingly, positive peptide shifts (open squares) are obtained for all amide-I modes in model B1, in contrast to the predictions in B2 and B3. This is counterintuitive, especially for the two amide-I modes at the second and third peptide linkages, because conformational analysis has shown that these two linkages are involved in intramolecular  $\beta_{10}$ -helical hydrogen bonding at both the  $\text{C}=\text{O}$  and  $\text{N}-\text{H}$  sites, and hydrogen bonding is expected to cause a red shift of the amide-I mode frequency.<sup>37–40</sup>

To discuss this discrepancy further, we analyzed the peptide contribution to the frequency shifts by separating it into three components based on their origins: the frequency shifts due to (i) the atoms involved in the intramolecular hydrogen bond (IHB) at the  $\text{C}=\text{O}$  and (ii)  $\text{N}-\text{H}$  sites and (iii) the other atoms on the side chains and backbone. The average values of these three components and their standard deviations are listed in Table 4. This separation was achieved by turning off contributions from the noninvolved atoms. For example, the frequency shift coming from hydrogen bonding at the carbonyl site was evaluated by setting zero charges to all atoms except for the N

and H atoms that are involved in forming the  $\beta_{10}$ -helical hydrogen bond. This analysis shows that the shifts due to IHB at the  $\text{N}-\text{H}$  site is positive in B1, and so is that at the  $\text{C}=\text{O}$  site in B2. Such a behavior contradicts the previous results that the amide-I frequency decreases when forming hydrogen bonds at the carbonyl and amide sites.<sup>37,39,40</sup>

Although red shifts at the  $\text{C}=\text{O}$  and  $\text{N}-\text{H}$  sites are correctly predicted in B3, the magnitude of the former is much smaller than that of the latter, inconsistent with the calculation results.<sup>37,39,40</sup> Overall, the positive peptide shifts compensate the negative solvent shifts, and the total frequency shifts (solid circles) obtained in the model B1 range from  $-11$  to  $1 \text{ cm}^{-1}$  with standard deviations of  $9$ – $11 \text{ cm}^{-1}$ . For models B2 and B3, the total shifts of the amide-I mode are  $-8$  to  $-20 \text{ cm}^{-1}$  and  $-15$  to  $-27 \text{ cm}^{-1}$ , respectively, and the fluctuations of  $5$ – $8 \text{ cm}^{-1}$  are smaller than those in B1.

Figure 7 shows that the total shifts of the amide-II modes in all models are dominated by the peptide shifts. It should be noted that in B1–B3, the solvent contribution leads to a redshift of the amide-II mode frequency, contradictory to the blueshift observed for amide compounds in chloroform.<sup>85</sup> When compared to B1, the frequency shifts calculated with models B2 and B3 exhibit much larger peptide contributions (more than  $50 \text{ cm}^{-1}$ ) and larger deviations (Table 2). The shifts due to the IHB partners and side chain atoms are very large in B2 and B3 (Table 4). The blueshift due to hydrogen bond formation is compensated by the redshift originating from other atoms, and the total peptide shifts become  $30$ – $99 \text{ cm}^{-1}$  in B1–B3. For the amide-II mode, previous calculation results predicted that hydrogen bonding at the  $\text{N}-\text{H}$  site causes a much larger blueshift than at the  $\text{C}=\text{O}$  site.<sup>39,40</sup> Of the three Bouř maps, only the results from B1 agree with this prediction.

For model K, the general trend for the variation of the total amide-I and -II frequency shifts across the peptide is similar to that of B3, but the magnitudes of the amide-II frequency shifts are much smaller (Figure 7). The hydrogen bonding effects at the  $\text{C}=\text{O}$  and  $\text{N}-\text{H}$  sites show the correct trend in both modes, in contrast to B3. However, the amide-I shifts of  $-6$  to  $-9 \text{ cm}^{-1}$  at the  $\text{C}=\text{O}$  site and  $-2$  to  $-6 \text{ cm}^{-1}$  at the  $\text{N}-\text{H}$  site are relatively small compared to the calculated values of about  $-20$  and about  $-10 \text{ cm}^{-1}$ .<sup>37,39</sup> The amide-II shifts due to the backbone and side chains are larger than the hydrogen bond shifts of  $2$ – $3 \text{ cm}^{-1}$  in this field/gradient model.

As mentioned in Methods, we tested two additional definitions of chromophore for this model (KN and KC). The solvent frequency shifts are not affected by the definition of chromophore. On the other hand, the peptide and total shifts in KN and KC are quite different from those in K (Figure 7 and Table 2). For example, some amide-I local modes show positive shifts, and negative shifts are seen for all of the amide-II modes. The acute chromophore dependence indicates that the electric fields and their gradients created by the atoms neighboring peptide linkages significantly affect the local mode frequencies. The trend of total frequency shifts observed for KN and KC implies that the excitonic amide-I and -II bands in  $\text{CDCl}_3$  would show blue- and redshifts, respectively, from the peak frequency observed in the gas phase. This is totally opposite to what we observed in the FTIR spectrum. Therefore, we hereafter do not further consider models KN and KC in the calculation of linear and 2D IR spectra and comparisons with the other models.

The pattern of amide-I total frequency shifts calculated using model G is close to that of K but with a smaller magnitude, about  $-11$  to  $-18 \text{ cm}^{-1}$ . In addition, the trend of hydrogen bonding effects is correctly predicted in this model except for

**TABLE 4:** Amide-I and -II Local Mode Frequency Shifts Due to the Intramolecular Hydrogen Bonding (IHB) Partners at the C=O and N–H Sites and the Other Atoms in the Backbone and Side Chains (BS)

model	linkage	amide-I frequency shift <sup>a</sup>					amide-II frequency shift <sup>a</sup>				
		1	2	3	4	5	1	2	3	4	5
B1	IHB (C=O)	-18.3 (1.9)	-17.6 (3.1)	-20.9 (5.8)			26.9 (1.3)	26.2 (1.8)	27.5 (3.5)		
	IHB (N–H)		11.4 (5.3)	3.0 (5.2)	5.8 (5.9)	7.2 (5.3)		33.9 (10.8)	51.4 (12.0)	55.0 (11.9)	43.1 (13.1)
	BS	27.7 (6.9)	15.7 (9.2)	21.4 (11.5)	8.6 (9.7)	10.2 (7.8)	3.8 (5.7)	-12.8 (12.5)	-41.0 (14.0)	-16.5 (12.6)	-5.9 (14.0)
	IHB (C=O)	2.9 (4.0)	1.7 (5.1)	7.5 (7.7)			146.9 (13.8)	138.5 (12.8)	138.2 (12.3)		
	IHB (N–H)		-32.9 (5.7)	-31.9 (6.2)	-37.2 (6.9)	-33.0 (6.5)		92.1 (22.0)	169.6 (24.5)	184.6 (26.3)	160.1 (34.6)
B2	BS	-3.2 (3.9)	20.6 (11.0)	18.8 (14.3)	38.0 (11.0)	17.7 (9.3)	-111.6 (18.3)	-154.1 (27.2)	-236.2 (28.2)	-96.0 (28.3)	-60.8 (34.1)
	IHB (C=O)	-14.3 (6.8)	-16.4 (7.9)	-8.7 (9.6)			223.3 (19.5)	211.4 (18.0)	211.2 (17.9)		
	IHB (N–H)		-44.4 (7.9)	-50.5 (9.2)	-56.2 (9.3)	-47.3 (10.2)		128.2 (32.6)	242.5 (35.2)	262.3 (37.6)	227.6 (50.3)
	BS	5.3 (4.8)	41.5 (8.2)	40.7 (10.3)	45.3 (8.0)	35.7 (9.0)	-165.1 (22.4)	-251.8 (38.5)	-388.6 (40.1)	-195.6 (39.0)	-159.9 (50.0)
	K	IHB (C=O)	-7.7 (2.3)	-8.5 (2.6)	-5.9 (2.9)		3.1 (1.2)	3.2 (1.4)	1.9 (1.4)		
G	IHB (N–H)		-4.5 (4.0)	-5.6 (4.4)	-1.7 (6.3)	-3.4 (4.1)		2.8 (1.8)	3.2 (2.0)	1.7 (2.8)	3.0 (2.1)
	BS	-9.6 (4.0)	-9.2 (4.1)	-7.8 (4.3)	-3.2 (4.6)	-5.0 (4.7)	10.7 (2.5)	10.8 (2.7)	9.0 (3.0)	7.5 (2.9)	8.2 (2.5)
	IHB (C=O)	-5.9 (2.6)	-7.0 (2.9)	-5.2 (3.0)			0.9 (1.0)	0.6 (1.3)	-0.1 (1.8)		
	IHB (N–H)		-1.3 (1.9)	-2.0 (2.0)	-1.3 (2.3)	-0.4 (1.9)		24.1 (4.6)	28.0 (5.3)	31.9 (5.4)	26.8 (5.7)
	BS	-2.2 (3.1)	-3.2 (3.5)	-3.1 (2.8)	2.3 (3.1)	-3.0 (3.0)	10.6 (5.4)	10.1 (5.2)	5.2 (5.3)	5.6 (5.3)	3.2 (5.0)

<sup>a</sup> The frequency shift (in  $\text{cm}^{-1}$ ) is averaged over 15 000 snapshots along the 1.5-ns MD trajectory. The numbers in parentheses represent the standard deviations of the frequency shifts.

the relatively smaller magnitudes than the reported theoretical values, just as in model K. The analysis for the amide-I mode suggests that the frequency correlation with the electrostatic properties is better parametrized at the four-atom sites, as in models K and G, rather than at the six sites in models B1–B3, in terms of reproducing the proper hydrogen bonding effects. Although the magnitude of the total amide-II frequency shift in model G is similar to that obtained with B1, particulars of the peptide shift are quite different. The solvent shifts of the amide-II mode in this model are positive, in contrast to B1–B3 but consistent with the trend found in the experiments.<sup>85</sup> It is noted that the total amide-II local frequency of the first linkage is always lower than the other linkages in the electrostatic potential-based models (B1, B2, B3, and G). This tendency is not seen in the field/gradient-based model K.

Finally, let us inspect the shifts obtained with our semiempirical model. Despite its simplicity, the calculated shifts resemble some of the electrostatic models. The amide-I modes have negative shifts of  $-20$  to  $-31 \text{ cm}^{-1}$ , and their pattern is similar to that of B3, K, and G. Comparing to B1 and G, the amide-II total frequency shifts are slightly smaller in magnitude by about  $10 \text{ cm}^{-1}$  (except for the first residue). The total frequency shifts obtained for the 1.5-ns MD trajectory are very similar to those calculated in the model calculation for the ideal  $3_{10}$ -helix in the previous work,<sup>34</sup> most likely because the molecular conformation of **1** acquired from the MD simulation is quite close to the ideal structure we assumed.

**C. Comparisons of Linear and 2D IR Spectra of the Unlabeled Peptide.** Figure 8 shows linear IR spectra of **1** measured<sup>34</sup> (black) and simulated using the six models (red). The unlabeled hexapeptide exhibits the urethane/ester C=O band at  $1716 \text{ cm}^{-1}$  and the unlabeled amide-I band at  $1666 \text{ cm}^{-1}$ . Roughly speaking, the two bands at  $1528$  and  $1498 \text{ cm}^{-1}$  can

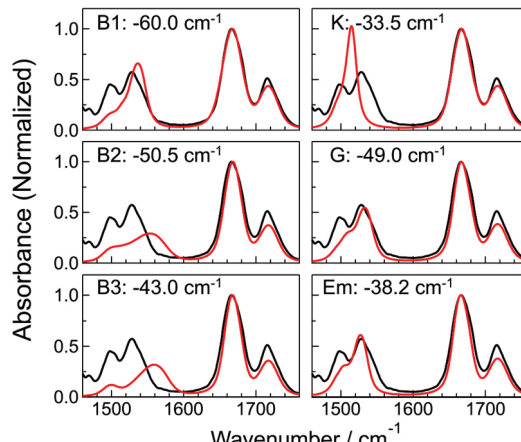


**Figure 8.** Experimental<sup>34</sup> (black) and simulated (red) linear IR spectra of the unlabeled peptide **1** in  $\text{CDCl}_3$ . Each spectrum is normalized by the peak intensity of the amide-I band at  $\sim 1660 \text{ cm}^{-1}$ . The local amide-I frequency was shifted from the gas phase value by the value reported in each panel to make the peak position of the amide-I exciton band coincide with that of the experimental spectrum.

be attributed to the vibrational exciton bands of the intramolecularly hydrogen-bonded amide-II modes and the free amide-II mode, respectively, with the latter being overlapped with the urethane-II mode.<sup>12,34</sup> For comparison, the frequency origin of the amide-I local mode was shifted from the gas phase value by the values reported in each panel of Figure 8 so that the peak of the simulated amide-I exciton band overlaps with the experimental peak. The origin shifts greatly depend on the model:  $-60.0 \text{ cm}^{-1}$  (B1),  $-50.5 \text{ cm}^{-1}$  (B2),  $-43.0 \text{ cm}^{-1}$  (B3),  $-33.5 \text{ cm}^{-1}$  (K),  $-49.0 \text{ cm}^{-1}$  (G), and  $-38.2 \text{ cm}^{-1}$  (Em). Overall, the observed amide-I band was reproduced quite well,

especially by B1 and K. The other models predict a slightly narrower (by  $\sim 6 \text{ cm}^{-1}$ ) band, and hence, the relative peak intensity ratio between the amide-I and the capping C=O bands varies. However, considering that B1 predicts a positive amide-I frequency shift upon forming a C=O $\cdots$ H–N intramolecular hydrogen bond and requires the largest shift of the origin, it is not appropriate to advocate that this model can simulate the amide-I spectrum well.

For the free and hydrogen-bonded amide-II bands, none of the models simulated the observed line shape to the same level as the amide-I mode. Models G and Em generate an intensity ratio close to that of the measurement, but the line widths are slightly narrower, and peaks are not as well resolved. The lower frequency band in the B1 simulated spectrum is quite small. The higher frequency band in B2 and B3 is very broad and is located at 1553 and 1559  $\text{cm}^{-1}$ , higher by about 25 and 31  $\text{cm}^{-1}$ , respectively, from the observed band at 1528  $\text{cm}^{-1}$ . The model K exhibits one asymmetric peak at 1515  $\text{cm}^{-1}$  with quite strong peak intensity.

Bouř and co-workers found from their simulated linear spectra of NMA in water that a bigger basis set is required to obtain reasonable agreement between the experimental and simulated amide-I frequency and line width.<sup>52</sup> They also found that the application of the B3LYP functional resulted in improvement of the amide-II frequency, whereas the amide-I frequency shifts away from the experimental value.<sup>52</sup> These results reflect only the solvent contributions, and hence, the basis set and functional dependence may be different when the backbone and side chain atoms are taken into account in the calculation of polypeptides. The linear amide-I band (Figure 8) of **1** simulated with B1, has a similar bandwidth to the experimental values. However, as mentioned above, this model with the lowest basis set (6-31G\*\*) is unable to predict the redshift of the local amide-I mode due to the intramolecular hydrogen bonding, and a quite large shift of the frequency origin ( $-60.0 \text{ cm}^{-1}$ ) is required. The calculated spectra with B2 and B3 have almost the same line width, and a slightly smaller frequency shift is needed for B3, which uses the B3LYP functional. This tendency of peak shift is different from that concluded for the amide-I band of NMA in water.<sup>52</sup>

A clear dependence on the basis set is noticeable for the simulated amide-II band. Comparing the results between B1 and B2, the higher basis set (B2) leads to a broader high-frequency amide-II band, with its frequency overestimated by  $\sim 25 \text{ cm}^{-1}$  from the experimental value. In B1, the high-frequency amide-II band is narrower than the measurement. The low-frequency peak position is relatively well reproduced to within a few  $\text{cm}^{-1}$ . In contrast, B2 and B3 use the same basis sets with a different functional. They give similar features for the amide-II band. Compared to the models B1–B3, the 6-31+G\* basis set used in the model G is relatively small, and the number of parametrized atoms is fewer. The amide-II band shape obtained from the model G is in reasonable agreement with the experiment. Interestingly, the lower basis set may be capable of reproducing the experimental results better. Keiderling and co-workers reported that a relatively small basis set [6-31G(d)] with the BPW91 functional was able to predict the amide-I and -II frequencies for the isolated and solvated NMA.<sup>38</sup> The dependence that Bouř et al. found in the calculation of NMA spectrum<sup>52</sup> was not reproduced once the DFT frequency maps were applied to the peptide linkages connected with one another through covalent bonds. These different trends most likely originate from contributions of peptide and backbone atoms.

The model K predicted the amide-I frequency and the bandwidth of linear spectrum better than any other models.

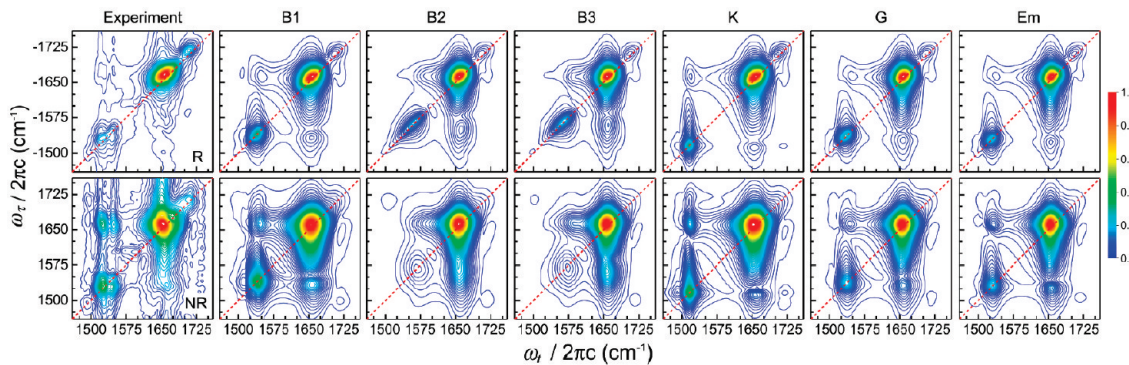
However, the high-frequency amide-II band is too narrow and the separation between the high- and low-frequency bands is so small that the overall band shape looks like a single peak with a marginal shoulder. Knoester and co-workers<sup>31</sup> simulated the linear IR spectrum of NMA-*d* in D<sub>2</sub>O on the basis of their frequency–field/gradient correlation and found that the calculated solvent shift of the amide-II mode ( $+21 \text{ cm}^{-1}$ ) is less than half of the experimental shift ( $+53 \text{ cm}^{-1}$ ). Another correlation based on electric field/gradient and second derivatives by Hayashi and Mukamei<sup>45</sup> also underestimated the solvent frequency shift of the amide-II band of undeuterated NMA, which was ascribed to insufficient electrostatic sampling. They also reported a similarly narrow amide-II band in the linear IR spectrum computed for a 17-residue helical peptide.<sup>78</sup> The amide-II mode frequency appears to be less well described by the field or gradient model.

In model G, the line shape of the amide-I band is almost the same as that simulated in B2 and B3. On the other hand, the amide-II band is not as broad as seen for the spectra of B2 and B3, rather close to that acquired in B1, and the intensity ratio between the high- and low-frequency bands is slightly better.

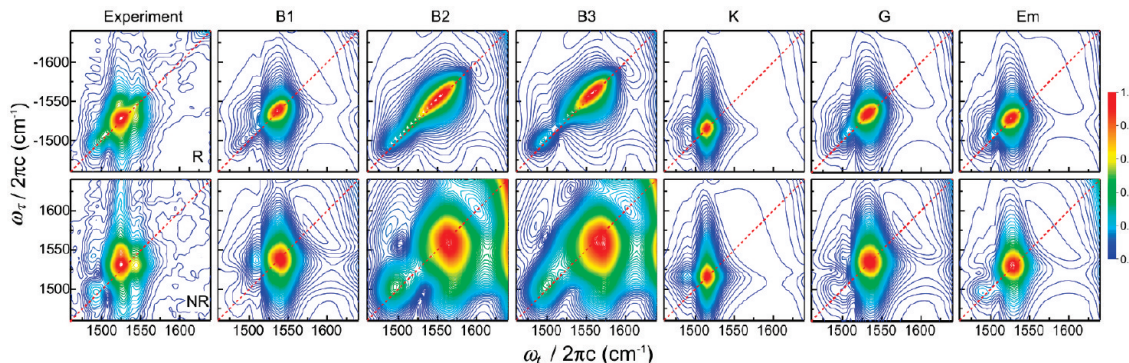
The semiempirical model Em could reproduce the measurement relatively well. The amide-I band is very similar to that in B2, B3 and G, and the two amide-II bands have a narrower line shape than the experimental result. In this model, the contributions of backbone and side chain atoms are completely ignored. The intramolecular C=O $\cdots$ H–N hydrogen bond and empirical solvent contributions are the sole sources that affect the site-energy of the amide-I and -II local modes. The total amide-II mode frequency in this model has the trend observed in the potential models, suggesting that the lower frequency in the first linkage can be attributed to the lack of intramolecular hydrogen bonding at the N–H group. It appears that the local amide-I and -II frequencies can be relatively well modeled by considering only a small number of atoms in the vicinity of peptide linkages. Kubelka and Keiderling<sup>38</sup> and Besley<sup>40</sup> reproduced the amide-I, -II and -III frequencies of NMA quite well by considering three explicit water molecules, two hydrogen-bonded at the carbonyl oxygen atom and one at the amide hydrogen atom, with continuum solvent model. Although the peptide linkage of NMA is fully solvated in water, the situation is different for the linkages connected with others in polypeptide chains to form a certain secondary structure. In the sample we studied, the hydrogen-bonded peptide units are surrounded by the methyl groups attached on the C<sup>α</sup> carbons and weakly polar chloroform molecules. These atom groups do not form strong hydrogen bonds with the C=O and N–H groups, and hence, the 3<sub>10</sub>-helical intramolecular hydrogen bonds would play a major role in affecting the local frequencies of the amide modes.

Figure 9 presents the measured<sup>34</sup> and simulated absolute magnitude 2D IR R and NR spectra of **1** in the full spectral region. The measured R spectrum exhibits a strong unlabeled amide-I peak, a urethane/ester C=O peak, and the amide-II peaks on the diagonal, corresponding to the prominent features in its linear spectrum. The hydrogen-bonded amide-II band at 1530–1550  $\text{cm}^{-1}$  is composed of several coupled peaks. The free amide-II band is a weak shoulder to the red side of the hydrogen-bonded amide-II band and cannot be clearly resolved. There are weak cross-peaks between the amide-I and hydrogen-bonded amide-II modes at  $\omega_t = 1525$  and 1548  $\text{cm}^{-1}$  along  $\omega_r = -1673 \text{ cm}^{-1}$ , but the cross-peaks between the amide-I and free amide-II modes are not discernible.

In contrast, the NR spectrum manifests better resolved diagonal peaks and more distinct cross-peaks than the R



**Figure 9.** Experimental<sup>34</sup> and simulated absolute magnitude 2D IR spectra of **1** obtained under the perpendicular polarization configuration: R (top); NR (bottom). Each spectrum is normalized by the amide-I peak intensity. The experimental and simulated spectra are plotted with 40 and 80 equally spaced contour lines, respectively.



**Figure 10.** Experimental<sup>12,34</sup> and simulated absolute magnitude 2D IR spectra of **1** in the amide-II frequency region: R (top) and NR (bottom). Each spectrum is normalized by the peak intensity of the diagonal amide-II band and plotted with 40 equally spaced contour lines.

spectrum. The NR sequence has higher resolving power due to destructive interference effects.<sup>32</sup> The two clear cross-peaks between the amide-I and -II modes along  $\omega_r = 1662 \text{ cm}^{-1}$  imply that the hydrogen-bonded amide-II band has two components, and each of them is coupled with the unlabeled amide-I modes. The free amide-II mode diagonal peak now clearly appears, and its cross-peaks to the hydrogen-bonded amide-II modes and amide-I modes are also much more clearly resolved.

For the simulated R and NR spectra, all models produced a diagonal amide-I band that resembles the experimental results, and thus, it is difficult to use this band as the criterion to compare different models. This behavior is consistent with the results from our previous study of a  $3_{10}$ -helical octapeptide: The linear spectra and parallel polarization 2D spectra are much less sensitive to the different electrostatic models than the amide-I 2D cross-peak patterns obtained by removing the diagonal peaks with the double-crossed polarization configuration.<sup>13</sup> Some cross-peaks between the amide-I and -II modes clearly show up in the simulated spectra, although those that originate from the shoulder of the amide-II band, which shows up in the off-diagonal region ( $\omega_r, \omega_t = (1661, 1549) \text{ cm}^{-1}$ ) of the measured NR spectrum, are not reproduced.

To investigate the amide-II band more clearly, the measured<sup>12,34</sup> and simulated spectra with the IR pulses centered at  $1550 \text{ cm}^{-1}$  are plotted in Figure 10. The spectra are normalized with the maximum intensity of the strongest diagonal amide-II band. Although the higher frequency shoulder is missing in all of the model simulations, qualitative reproduction of the experimental results is achieved by B1, G, and Em. As deduced from the simulated linear spectra, the diagonal amide-II band in B2 and B3 is highly broadened along the diagonal direction, indicating that the inhomogeneity of the local amide-II mode is quite large in these models. Model K generates a narrower diagonal band

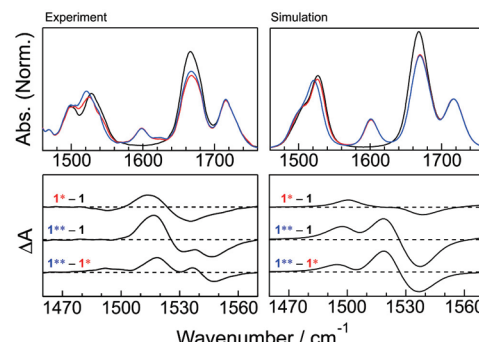


**Figure 11.** Experimental<sup>34</sup> (top left) and simulated (top right) linear IR spectra of **1** (black), **1\*** (red), and **1\*\*** (blue) in  $\text{CDCl}_3$ . Each spectra is normalized by the peak intensity of the urethane/ester  $\text{C}=\text{O}$  band at  $\sim 1716 \text{ cm}^{-1}$  after subtracting the background spectrum of neat  $\text{CDCl}_3$ . Experimental<sup>12,34</sup> (bottom left) and simulated (bottom right) difference spectra between **1\*** and **1**, **1\*\*** and **1**, and **1\*\*** and **1\***.

with a clear cross-peak between the lower and higher frequency band. Comparing to the amide-I mode, simulation of the amide-II mode exhibits larger spectral variations between different models.

**D. Simulated Linear and 2D IR Spectra of **1\*** and **1\*\***.** For further simulation of the isotope labeled peptides **1\*** and **1\*\***, we have chosen models K and G, which relatively well reproduced the amide-I and -II profiles of **1**, respectively. Figure 11 shows the measured<sup>12,34</sup> and simulated linear IR spectra after normalization with the band intensity of the urethane/ester  $\text{C}=\text{O}$  band at  $\sim 1716 \text{ cm}^{-1}$ , a common internal reference band for the spectra of **1**, **1\***, and **1\*\***, as well as the difference spectra of  $\mathbf{1^* - 1}$ ,  $\mathbf{1^{**} - 1}$ , and  $\mathbf{1^{**} - 1^*}$ . A new band at  $1598 \text{ cm}^{-1}$  is due to the  $^{13}\text{C} = ^{18}\text{O}$  labeled amide-I band in the second linkage. Again, the simulated labeled and unlabeled amide-I

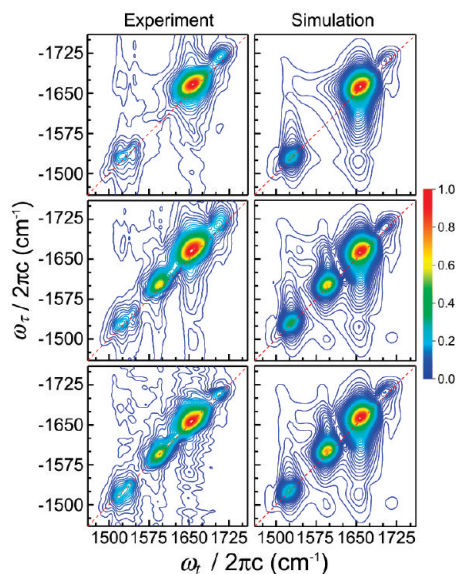


**Figure 12.** Experimental<sup>34</sup> (left) and simulated (right) absolute magnitude 2D IR R spectra obtained under the perpendicular polarization configuration: **1** (top), **1\*** (middle), and **1\*\*** (bottom). The simulation was carried out using models K and G for the amide-I and II modes, respectively. Each spectrum is normalized by the maximum intensity of the unlabeled amide-I peak. The experimental and simulated spectra are plotted with 40 and 80 equally spaced contour lines, respectively.

band is slightly narrower than the measured one. The effects of  $^{13}\text{C}=\text{O}$  and  $^{15}\text{N}$  on the amide-II mode are clearly observed in the difference spectra. The complicated difference profiles were only partially replicated. In the difference spectrum between **1\*** and **1**, the positive and negative couplet are more separated in frequency. The increased absorbance at  $\sim 1518 \text{ cm}^{-1}$  by the  $^{15}\text{N}$  label was reproduced in the simulated difference spectra  $\mathbf{1}^{**} - \mathbf{1}$  and  $\mathbf{1}^{**} - \mathbf{1}^*$ . The increase at  $1495 \text{ cm}^{-1}$  is overestimated, and the decreased absorbance between  $1530$  and  $1550 \text{ cm}^{-1}$  is different from the experimental results. These discrepancies require further refinement.

Figures 12 and 13 show the measured<sup>34</sup> and simulated absolute magnitude 2D IR R and NR spectra, respectively, with the IR pulses centered at  $1600 \text{ cm}^{-1}$ . The spectra at  $1550 \text{ cm}^{-1}$ , including the  $^{13}\text{C}=\text{O}$  labeled amide-I and amide-II bands, are plotted in Figures 14 and 15. The top panels in Figure 15 show the sliced NR spectra at  $\omega_t = 1598 \text{ cm}^{-1}$ . In the previous studies,<sup>12,34</sup> it has been demonstrated that a combination of the  $^{13}\text{C}=\text{O}$  label on the amide-I mode and the  $^{15}\text{N}$  label on the amide-II mode is able to select out a specific amide-I/II cross-peak from among the others, as featured in the cross-peak of **1\*\*** at  $\omega_t \sim 1520 \text{ cm}^{-1}$  that is red-shifted by about  $9 \text{ cm}^{-1}$  from the cross-peak of **1\*** (Figure 15, left-top panel). The simulation in this study resulted in a smaller red shift ( $5 \text{ cm}^{-1}$ ). The cross-peak intensity between the  $^{13}\text{C}=\text{O}$  amide-I and hydrogen-bonded amide-II mode for the mono- and bis-labeled peptides is not as strong as the measured one.

The disagreement with the experimental results suggests that improvements on the simulation of amide 2D IR spectra are needed. For example, it is still an open question how the vibrational coupling strength between the amide-I and -II modes is affected by the intramolecular  $\text{C}=\text{O} \cdots \text{H}-\text{N}$  hydrogen bond connecting them in a helical structure, and it might be quite different from the transition charge coupling assumed in our simulation. The amide-I/II nearest neighbor coupling estimated by us<sup>34</sup> and other groups<sup>33,53</sup> needs to be experimentally verified

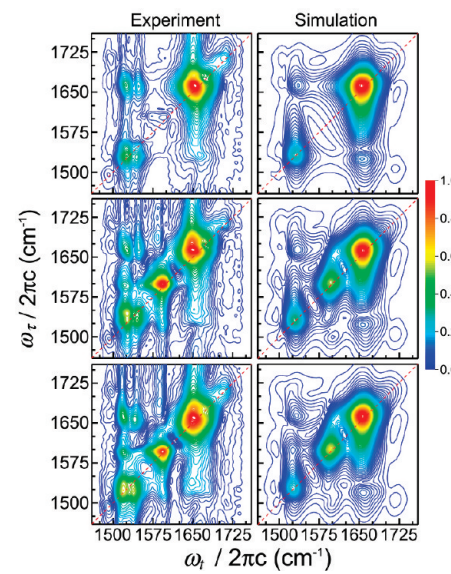


**Figure 13.** Experimental<sup>34</sup> (left) and simulated (right) absolute magnitude 2D IR NR spectra (right): **1** (top), **1\*** (middle), and **1\*\*** (bottom). See the caption of Figure 12 for other details.

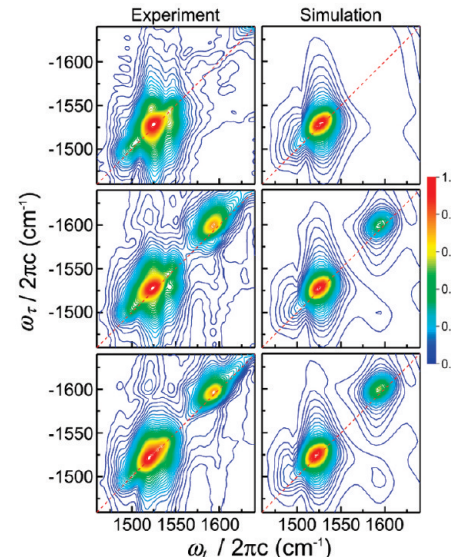


**Figure 14.** Experimental<sup>12,34</sup> (left) and simulated (right) absolute magnitude 2D IR R spectra in the amide-II frequency region: **1** (top), **1\*** (middle), and **1\*\*** (bottom). Each spectrum is normalized by the maximum intensity of the diagonal amide-II band and plotted with 40 equally spaced contour lines.

for various peptide conformations. The spatial extent and conformational dependence of the amide-II/II couplings also require further experimental determination.<sup>33,34,36</sup> The electrostatic model calculations in this study chose the chromophore definitions that maintain charge neutrality. A recent study employed another definition that removes the atoms that are away by three covalent bonds from the parametrized sites.<sup>47</sup> Further systematic study is required to clarify the effects of chromophore definition.

#### IV. Concluding Remarks

Our comparative study of different electrostatic and semiempirical models has revealed several intriguing points. The simulated amide-I bands obtained from all models are very similar in their line widths and closely resemble the experimental data, except that the frequency redshifts required to overlap with

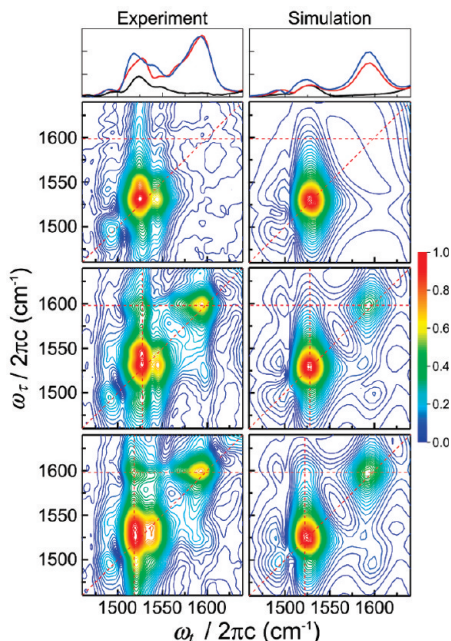


**Figure 15.** Experimental<sup>12,34</sup> (left) and simulated (right) absolute magnitude 2D IR NR spectra in the amide-II frequency region: **1** (top), **1\*** (middle), and **1\*\*** (bottom). Each spectrum is normalized by the maximum intensity of the diagonal amide-II band and plotted with 40 equally spaced contour lines. Slices of the 2D spectra at  $\omega_r = 1598 \text{ cm}^{-1}$  for **1** (black), **1\*** (red), and **1\*\*** (blue) are plotted in the top panels.

the experiment are quite different between the models. However, the six-site models may be less suitable for modeling the amide-I and -II local mode frequencies in peptides and proteins because it cannot properly describe the hydrogen bonding effects on the frequencies. In contrast to the model insensitivity observed in the amide-I mode, the six models led to drastically different amide-II bands in the linear and 2D IR spectra. On the basis of the five electrostatic models studied here, the average and fluctuations of the amide-II local site-energy appear to be better computed when it is correlated with the electrostatic potential, rather than the electric field and gradient, created by the atoms surrounding the peptide linkages. In addition, a larger basis set does not necessarily generate a more accurate DFT frequency map, at least for the amide-II mode. Model G, based on a relatively small basis set, performs reasonably well. Despite the simplicity of our semiempirical model, which takes into account only the intramolecular hydrogen bonding effects and empirical solvent shifts, it is able to reproduce many of the amide-I/II spectral features. This indicates that hydrogen bonding effects in the vicinity of the peptide unit need to be carefully modeled to accurately estimate the site energy of the amide-I and amide-II modes. Further refinements of the modeling are needed to obtain more quantitative agreement and better estimation of the isotope effects on the amide-II spectral profiles. Given that vibrational couplings and correlations among different amide modes contain a wealth of information on peptide structure and dynamics, improvements in theoretical modeling and comprehensive comparisons between experimental and simulated amide 2D IR spectra will be essential to successful extraction of such information.

**Acknowledgment.** This research was supported by a grant from the National Science Foundation (CHE-0450045).

## References and Notes

- (1) Krimm, S.; Bandekar, J. *Adv. Protein Chem.* **1986**, *38*, 181.
- (2) Barth, A.; Zscherg, C. *Q. Rev. Biophys.* **2002**, *35*, 369.
- (3) Keiderling, T. A. *Curr. Opin. Chem. Biol.* **2002**, *6*, 682.
- (4) Hochstrasser, R. M. *Proc. Natl. Acad. Sci. U.S.A.* **2007**, *104*, 14190.
- (5) Cho, M. *Chem. Rev.* **2008**, *108*, 1331.
- (6) Zhuang, W.; Hayashi, T.; Mukamel, S. *Angew. Chem., Int. Ed.* **2009**, *48*, 3750.
- (7) Woutersen, S.; Hamm, P. *J. Chem. Phys.* **2001**, *115*, 7737.
- (8) Fang, C.; Wang, J.; Kim, Y. S.; Charnley, A. K.; Barber-Armstrong, W.; Smith, A. B., III; Decatur, S. M.; Hochstrasser, R. M. *J. Phys. Chem. B* **2004**, *108*, 10415.
- (9) Maekawa, H.; Toniolo, C.; Moretto, A.; Broxterman, Q. B.; Ge, N.-H. *J. Phys. Chem. B* **2006**, *110*, 5834.
- (10) Maekawa, H.; Toniolo, C.; Broxterman, Q. B.; Ge, N.-H. *J. Phys. Chem. B* **2007**, *111*, 3222.
- (11) Maekawa, H.; Formaggio, F.; Toniolo, C.; Ge, N.-H. *J. Am. Chem. Soc.* **2008**, *130*, 6556.
- (12) Maekawa, H.; De Poli, M.; Toniolo, C.; Ge, N.-H. *J. Am. Chem. Soc.* **2009**, *131*, 2042.
- (13) Sengupta, N.; Maekawa, H.; Zhuang, W.; Toniolo, C.; Mukamel, S.; Tobias, D. J.; Ge, N.-H. *J. Phys. Chem. B* **2009**, *113*, 12037.
- (14) Demirdöven, N.; Cheatum, C. M.; Chung, H. S.; Khalil, M.; Knoester, J.; Tokmakoff, A. *J. Am. Chem. Soc.* **2004**, *126*, 7981.
- (15) Dijkstra, A. G.; Knoester, J. *J. Phys. Chem. B* **2005**, *109*, 9787.
- (16) Wang, J.; Chen, J.; Hochstrasser, R. M. *J. Phys. Chem. B* **2006**, *110*, 7545.
- (17) Smith, W. S.; Tokmakoff, A. *J. Chem. Phys.* **2007**, *126*, 045109.
- (18) Wang, J.; Zhuang, W.; Mukamel, S.; Hochstrasser, R. M. *J. Phys. Chem. B* **2008**, *112*, 5930.
- (19) Ganim, Z.; Chung, H. S.; Smith, A. W.; DeFlores, L. P.; Jones, K. C.; Tokmakoff, A. *Acc. Chem. Res.* **2008**, *41*, 432.
- (20) Mukherjee, P.; Kass, I.; Arkin, I. T.; Zanni, M. T. *Proc. Natl. Acad. Sci. U.S.A.* **2006**, *103*, 3528.
- (21) Kim, Y. S.; Liu, L.; Axelsen, P. H.; Hochstrasser, R. M. *Proc. Natl. Acad. Sci. U.S.A.* **2008**, *105*, 7720.
- (22) Strasfeld, D. B.; Ling, Y. L.; Shim, S.-H.; Zanni, M. T. *J. Am. Chem. Soc.* **2008**, *130*, 6698.
- (23) Hamm, P.; Helbing, J.; Bredenbeck, J. *Annu. Rev. Phys. Chem.* **2008**, *59*, 291.
- (24) Decatur, S. M. *Acc. Chem. Res.* **2006**, *39*, 169.
- (25) Arkin, I. T. *Curr. Opin. Chem. Biol.* **2006**, *10*, 394.
- (26) Mirkin, N. G.; Krimm, S. *J. Phys. Chem. A* **2002**, *106*, 3391.
- (27) Lee, S.-H.; Krimm, S. *Chem. Phys.* **1998**, *230*, 277.
- (28) Englander, S. W.; Sosnick, T. R.; Englander, J. J.; Mayne, L. *Curr. Opin. Struct. Biol.* **1996**, *6*, 18.
- (29) Rubtsov, I. V.; Wang, J.; Hochstrasser, R. M. *Proc. Natl. Acad. Sci. U.S.A.* **2003**, *100*, 5601.
- (30) DeFlores, L. P.; Ganim, Z.; Ackley, S. F.; Chung, H. S.; Tokmakoff, A. *J. Phys. Chem. B* **2006**, *110*, 18973.
- (31) Bloem, R.; Dijkstra, A. G.; Jansen, T. I. C.; Knoester, J. *J. Chem. Phys.* **2008**, *129*, 055101.
- (32) Sul, S.; Karauskaj, D.; Jiang, Y.; Ge, N.-H. *J. Phys. Chem. B* **2006**, *110*, 19891.
- (33) Hayashi, T.; Mukamel, S. *J. Phys. Chem. B* **2007**, *111*, 11032.
- (34) Maekawa, H.; De Poli, M.; Moretto, A.; Toniolo, C.; Ge, N.-H. *J. Phys. Chem. B* **2009**, *113*, 11775.
- (35) DeFlores, L. P.; Tokmakoff, A. *J. Am. Chem. Soc.* **2006**, *128*, 16520.
- (36) DeFlores, L. P.; Ganim, Z.; Nicodemus, R. A.; Tokmakoff, A. *J. Am. Chem. Soc.* **2009**, *131*, 3385.
- (37) Torii, H.; Tasumi, T.; Tasumi, M. *Mikrochim. Acta* **1997**, *14*, 531.
- (38) Kubelka, J.; Keiderling, T. A. *J. Phys. Chem. A* **2001**, *105*, 10922.
- (39) Kim, J.-H.; Cho, M. *Bull. Korean Chem. Soc.* **2003**, *24*, 1061.
- (40) Besley, N. A. *J. Phys. Chem. A* **2004**, *108*, 10794.
- (41) Ham, S.; Kim, J.-H.; Lee, H.; Cho, M. *J. Chem. Phys.* **2003**, *118*, 3491.
- (42) Bouř, P.; Keiderling, T. A. *J. Chem. Phys.* **2003**, *119*, 11253.
- (43) Schmidt, J. R.; Corcelli, S. A.; Skinner, J. L. *J. Chem. Phys.* **2004**, *121*, 8887.
- (44) Watson, T. M.; Hirst, J. D. *Mol. Phys.* **2005**, *103*, 1531.
- (45) Hayashi, T.; Zhuang, W.; Mukamel, S. *J. Phys. Chem. A* **2005**, *109*, 9747.
- (46) Jansen, T. I. C.; Knoester, J. *J. Chem. Phys.* **2006**, *124*, 044502.
- (47) Lin, Y. S.; Shorb, J. M.; Mukherjee, P.; Zanni, M. T.; Skinner, J. L. *J. Phys. Chem. B* **2009**, *113*, 592.
- (48) Torii, H.; Tasumi, M. *J. Raman Spectrosc.* **1998**, *29*, 81.
- (49) Hamm, P.; Woutersen, S. *Bull. Chem. Jpn.* **2002**, *75*, 985.
- (50) Gorbunov, R. D.; Kosov, D. S.; Stock, G. *J. Chem. Phys.* **2005**, *122*, 224904.
- (51) Jansen, T. I. C.; Dijkstra, A. G.; Watson, T. M.; Hirst, J. D.; Knoester, J. *J. Chem. Phys.* **2006**, *125*, 044312.
- (52) Bouř, P.; Michalik, D.; Kapitan, J. *J. Chem. Phys.* **2005**, *122*, 144501.
- (53) Choi, J.-H.; Cho, M. *Chem. Phys.* **2009**, *361*, 168.
- (54) Ganim, Z.; Tokmakoff, A. *Biophys. J.* **2006**, *91*, 2636.
- (55) Karle, I. L.; Balaram, P. *Biochemistry* **1990**, *29*, 6747.

- (56) Toniolo, C.; Benedetti, E. *Trends Biochem. Sci.* **1991**, *16*, 350.
- (57) Balaram, P. *Curr. Opin. Struct. Biol.* **1992**, *2*, 845.
- (58) Toniolo, C.; Polese, A.; Formaggio, F.; Crisma, M.; Kamphuis, J. *J. Am. Chem. Soc.* **1996**, *118*, 2744.
- (59) Yoder, G.; Polese, A.; Silva, R.; Formaggio, F.; Crisma, M.; Broxterman, Q. B.; Kamphuis, J.; Toniolo, C.; Keiderling, T. A. *J. Am. Chem. Soc.* **1997**, *119*, 10278.
- (60) Cornell, W. D.; Cieplak, P.; Bayly, C. I.; Gould, I. R.; Merz, K. M.; Ferguson, D. M.; Spellmeyer, D. C.; Fox, T.; Caldwell, J. W.; Kollman, P. A. *J. Am. Chem. Soc.* **1995**, *117*, 5179.
- (61) Wang, J.; Cieplak, P.; Kollman, P. A. *J. Comput. Chem.* **2000**, *21*, 1049.
- (62) Hormak, V.; Abel, R.; Okur, A.; Strockbine, B.; Roitberg, A.; Simmerling, C. *Proteins: Struct., Funct., Bioinf.* **2006**, *65*, 712.
- (63) Mahadevan, J.; Lee, K.-H.; Kuczera, K. *J. Phys. Chem. B* **2001**, *105*, 1863.
- (64) Bürgi, R.; Daura, X.; Mark, A.; van Gunsteren, W.; Bellanda, M.; Mammi, S.; Peggion, E. *J. Pept. Res.* **2001**, *57*, 107.
- (65) Botan, V.; Backus, E. H. G.; Pfister, R.; Moretto, A.; Crisma, M.; Toniolo, C.; Nguyen, P. H.; Stock, G.; Hamm, P. *Proc. Natl. Acad. Sci. U.S.A.* **2007**, *104*, 12749.
- (66) Zhang, L.; Hermans, J. *J. Am. Chem. Soc.* **1994**, *116*, 11915.
- (67) Phillips, J. C.; Braun, R.; Wang, W.; Gumbart, J.; Tajkhorshid, E.; Villa, E.; Chipot, C.; Skeel, R. D.; Kalé, L.; Schulten, K. *J. Comput. Chem.* **2005**, *26*, 1781.
- (68) Cieplak, P.; Cornell, W. D.; Bayly, C.; Kollman, P. A. *J. Comput. Chem.* **1995**, *16*, 1357.
- (69) Preto, M. A. C.; Melo, A.; Costa, S. P. G.; Maia, H. L. S.; Ramos, M. J. *J. Phys. Chem. B* **2003**, *107*, 14556.
- (70) Martyna, G. J.; Tobias, D. J.; Klein, M. L. *J. Chem. Phys.* **1994**, *101*, 4177.
- (71) Feller, S. E.; Zhang, Y.; Pastor, R. W.; Brooks, B. R. *J. Chem. Phys.* **1995**, *103*, 4613.
- (72) Darden, T.; York, D.; Pedersen, L. *J. Chem. Phys.* **1993**, *98*, 10089.
- (73) Ryckaert, J.-P.; Ciccotti, G.; Berendsen, H. J. C. *J. Comput. Phys.* **1977**, *23*, 327.
- (74) Frisch, M. J.; Trucks, G. W.; Schlegel, H. B.; Scuseria, G. E.; Robb, M. A.; Cheeseman, J. R.; Montgomery, J. A., Jr.; Vreven, T.; Kudin, K. N.; Burant, J. C.; Millam, J. M.; Iyengar, S. S.; Tomasi, J.; Barone, V.; Mennucci, B.; Cossi, M.; Scalmani, G.; Rega, N.; Petersson, G. A.; Nakatsuji, H.; Hada, M.; Ehara, M.; Toyota, K.; Fukuda, R.; Hasegawa, J.; Ishida, M.; Nakajima, T.; Honda, Y.; Kitao, O.; Nakai, H.; Klene, M.; Li, X.; Knox, J. E.; Hratchian, H. P.; Cross, J. B.; Bakken, V.; Adamo, C.; Jaramillo, J.; Gomperts, R.; Stratmann, R. E.; Yazyev, O.; Austin, A. J.; Cammi, R.; Pomelli, C.; Ochterski, J. W.; Ayala, P. Y.; Morokuma, K.; Voth, G. A.; Salvador, P.; Dannenberg, J. J.; Zakrzewski, V. G.; Dapprich, S.; Daniels, A. D.; Strain, M. C.; Farkas, O.; Malick, D. K.; Rabuck, A. D.; Raghavachari, K.; Foresman, J. B.; Ortiz, J. V.; Cui, Q.; Baboul, A. G.; Clifford, S.; Ciosowski, J.; Stefanov, B. B.; Liu, G.; Liashenko, A.; Piskorz, P.; Komaromi, I.; Martin, R. L.; Fox, D. J.; Keith, T.; Al-Laham, M. A.; Peng, C. Y.; Nanayakkara, A.; Challacombe, M.; Gill, P. M. W.; Johnson, B.; Chen, W.; Wong, M. W.; Gonzalez, C.; Pople, J. A. *Gaussian 03*; Gaussian, Inc.: Wallingford, CT, 2004.
- (75) Zhuang, W.; Abramavicius, D.; Hayashi, T.; Mukamel, S. *J. Phys. Chem. B* **2006**, *110*, 3362.
- (76) Rubtsov, I. V.; Hochstrasser, R. M. *J. Phys. Chem. B* **2002**, *106*, 9165.
- (77) Hamm, P.; Lim, M.; Hochstrasser, R. M. *J. Phys. Chem. B* **1998**, *102*, 6123.
- (78) Hayashi, T.; Mukamel, S. *J. Mol. Liq.* **2008**, *141*, 149.
- (79) Torii, H. *Chem. Phys. Lett.* **2005**, *414*, 417.
- (80) Auer, B. M.; Skinner, J. L. *J. Chem. Phys.* **2007**, *127*, 104105.
- (81) Jansen, T. I. C.; Knoester, J. *Acc. Chem. Res.* **2009**, *42*, 1405.
- (82) Kabsch, W.; Sander, C. *Biopolymers* **1983**, *22*, 2577.
- (83) Toniolo, C.; Crisma, M.; Bonora, G. M.; Benedetti, E.; Di Blasio, B.; Pavone, V.; Pedone, C.; Santini, A. *Biopolymers* **1991**, *31*, 129.
- (84) Kennedy, D. F.; Crisma, M.; Toniolo, C.; Chapman, D. *Biochemistry* **1991**, *30*, 6541.
- (85) Filliaux, F.; De Lozé, C. *Biopolymers* **1972**, *11*, 2063.

JP908695G